Supporting Information

Self-supported multidimensional Ni-Fe phosphide networks with holey nanosheets for high-performance all-solid-state supercapacitors

Shuo Li,[a] Minghao Hua,[a] Yuan Yang,[a] Wei Huang,[b] Xiaohang Lin,[a] Lijie Ci,[a] Jun Lou[c], Pengchao Si*[a]

[a] SDU & Rice Joint Center for Carbon Nanomaterials, Key Laboratory for Liquid-Solid Structural Evolution and Processing of Materials, Ministry of Education, School of Materials Science and Engineering, Shandong University, Jinan 250061, P. R. China
E-mail: pcsi@sdu.edu.cn
[b] Department of Chemistry, Technical University of Denmark, DK-2800 Kongens Lyngby, Denmark
[c] SDU & Rice Joint Center for Carbon Nanomaterials, Department of Materials Science and NanoEngineering, Rice University, Houston, TX 77005, USA

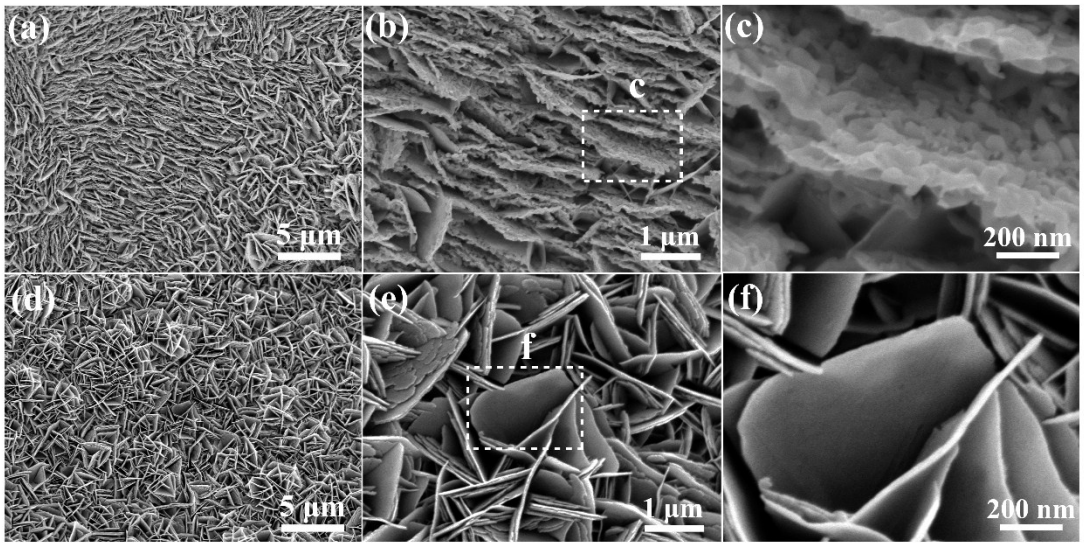

Fig. S1 SEM images with different magnifications of (a-c) Ni_2P network and (d-e) Ni-Fe-O network.

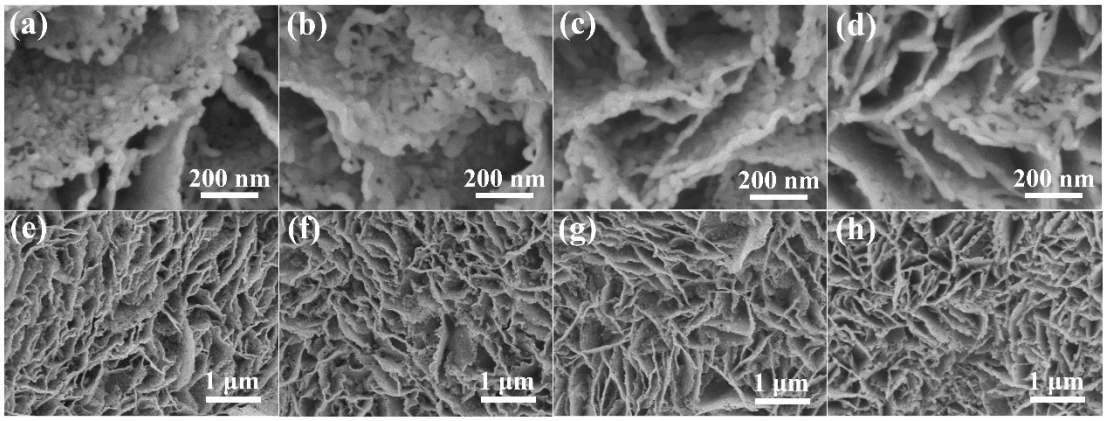

Fig. S2 SEM images with different magnifications of (a, e) NFP-1, (b, f) NFP-2, (c, g) NFP-4 and (d, h) NFP-5 electrodes.

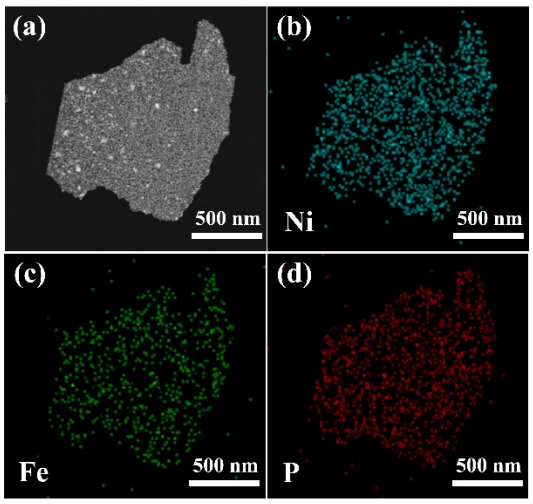

Fig. S3 a) STEM image of Ni-Fe-P-350 nanosheet and the corresponding EDS color elemental mappings of b) Ni-K, c) Fe-K, and d) P-K.

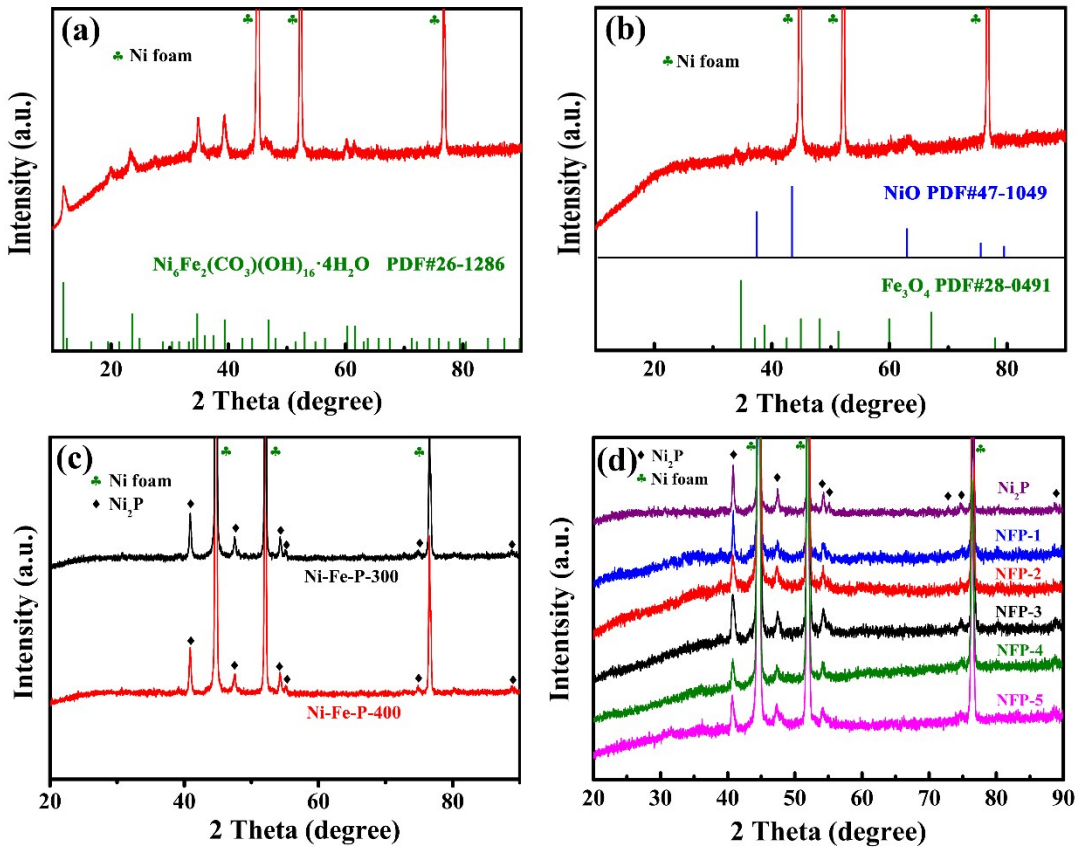

Fig. S4 XRD patterns of (a) Ni-Fe LDH and (b) Ni-Fe-O, and (c) Ni-Fe-P-300 and Ni-Fe-P-400, (d) NFP-1, -2, -3 (Ni-Fe-P-350), -4, -5, and Ni_2P electrodes.

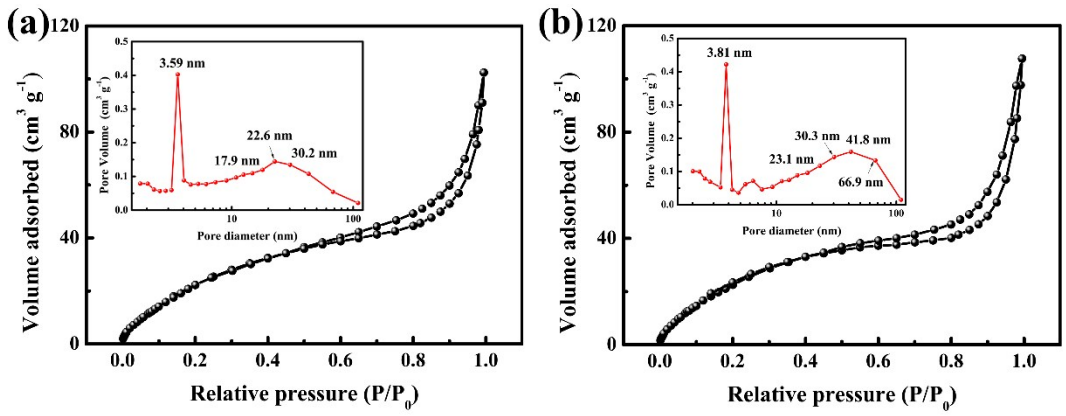

Fig. S5 Nitrogen adsorption-desorption isotherms of (a) Ni-Fe-P-300 and (b) Ni-Fe-P-400 electrodes (the insets show the corresponding pore size distributions).

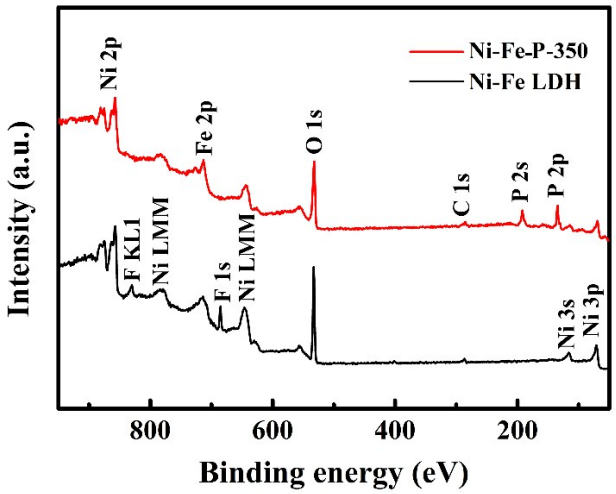

Fig. S6 XPS wide survey spectrums of Ni-Fe-P-350 and Ni-Fe LDH.

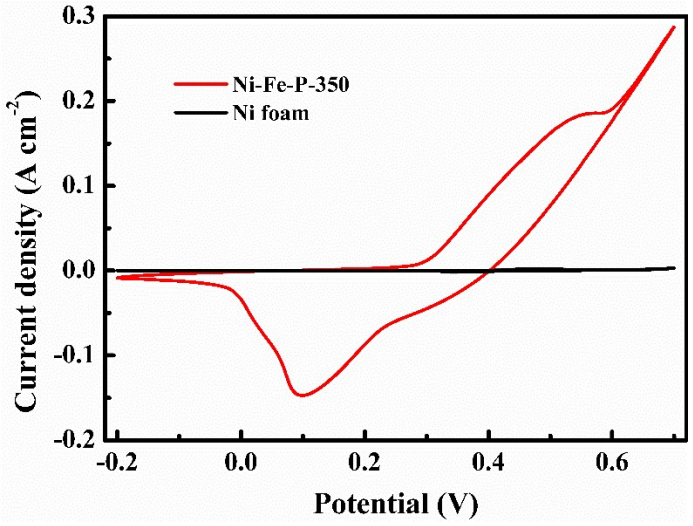

Fig. S7 CV tests of Ni-Fe-P-350 and pure Ni foam electrodes at 20 mV s^{-1}.

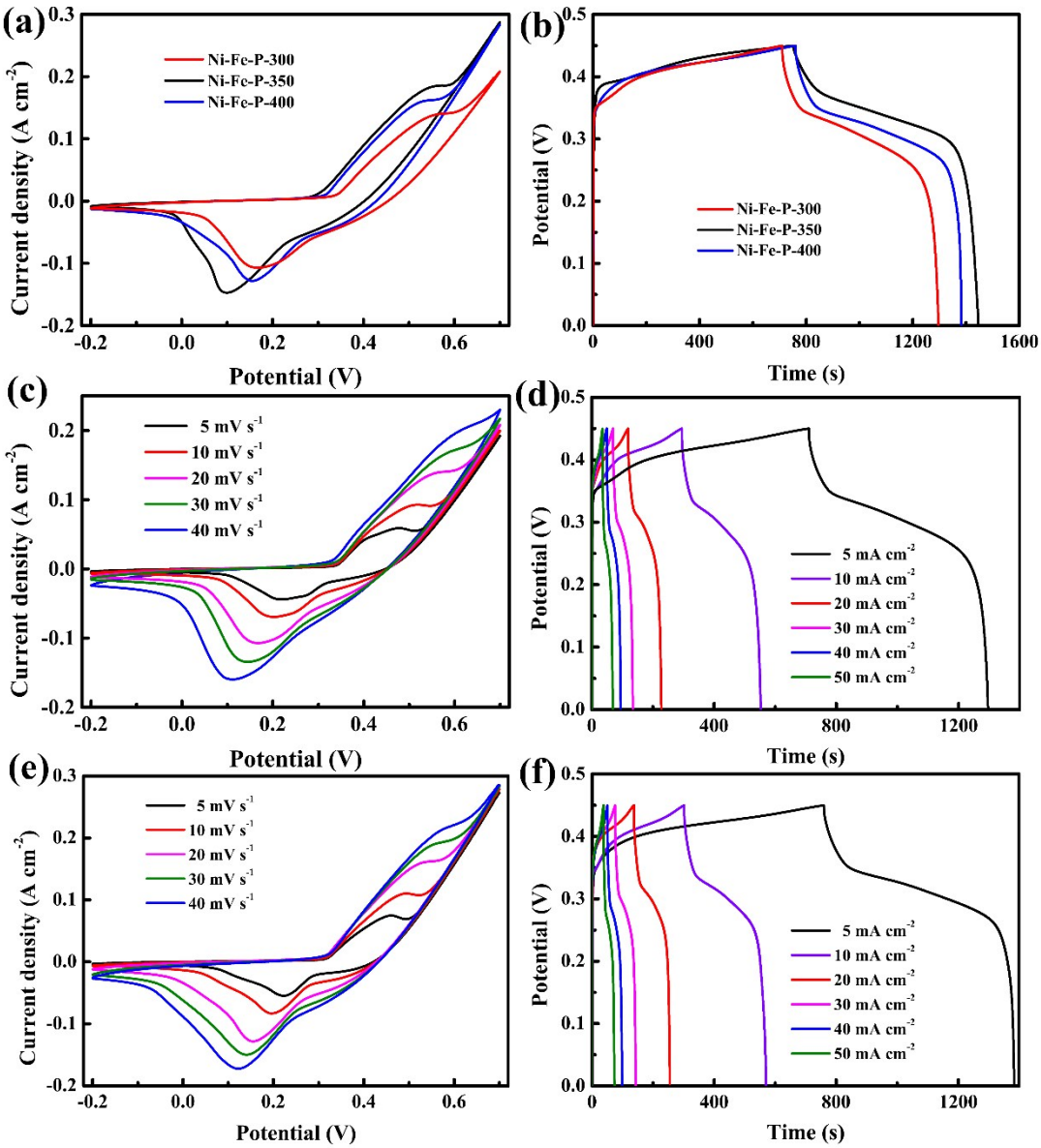

Fig. S8 (a) CV tests at 20 mV $s^{-1}$and (b) GCD tests at 5 mA cm^{-2} of Ni-Fe-P electrodes with different annealed temperatures (300, 350, and 400°C). (c) CV curves and (d) GCD curves of (c) Ni-Fe-P-300 electrode. (e) CV curves and (f) GCD curves of (c) Ni-Fe-P-400 electrode.

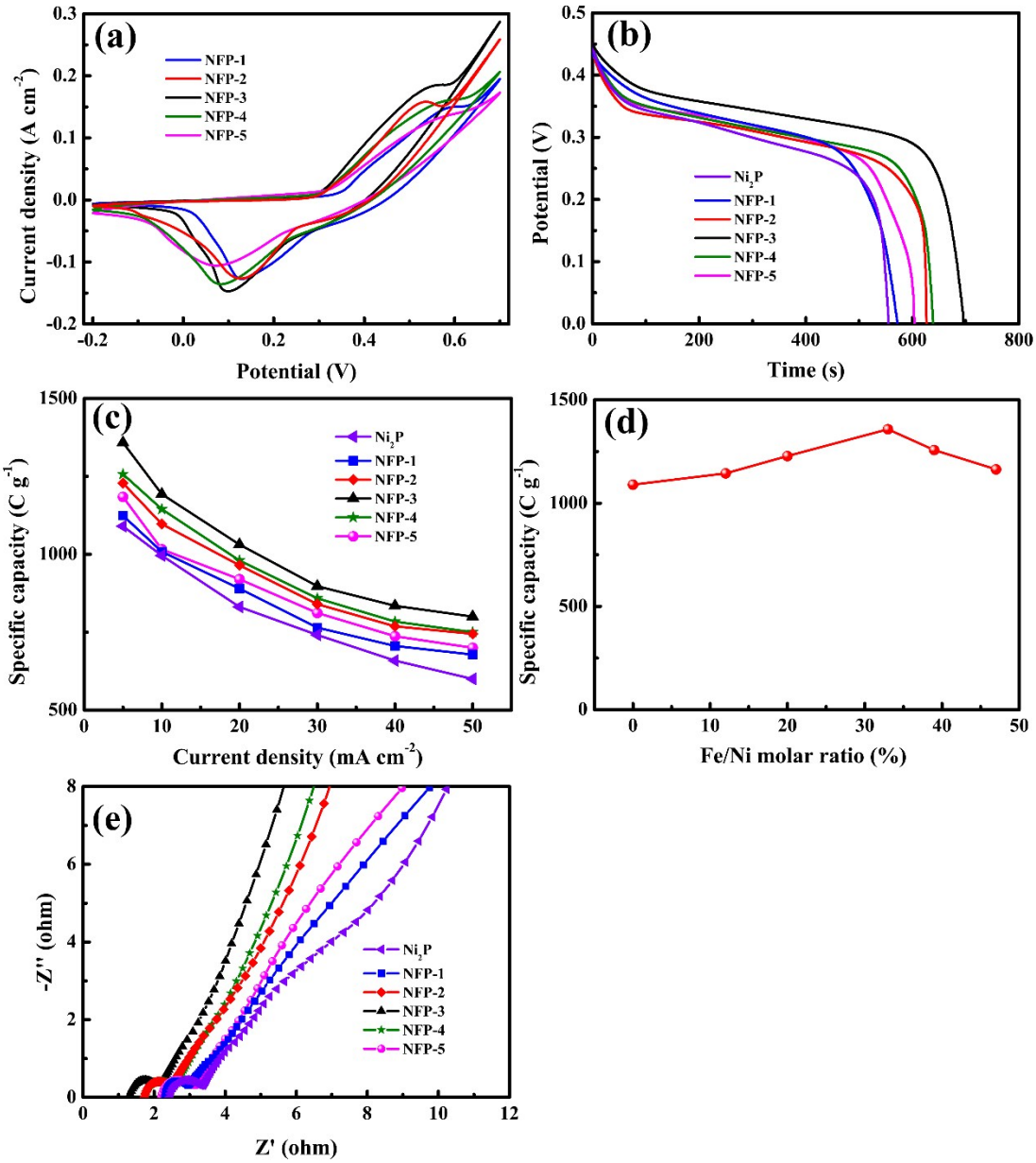

Fig. S9 (a) CV curves at the scan rate of 20 mV s^{-1}, (b) GCD curves at the current density of 5 mA cm^{-2}, (c) specific capacities at different current densities of NFP-1, -2, -3, -4, -5 and Ni_2P electrodes. (d) The plots of the relationship between specific capacity and Fe/Ni molar ratio. (e) EIS curves of NFP-1, -2, -3, -4, -5 and Ni_2P electrodes.

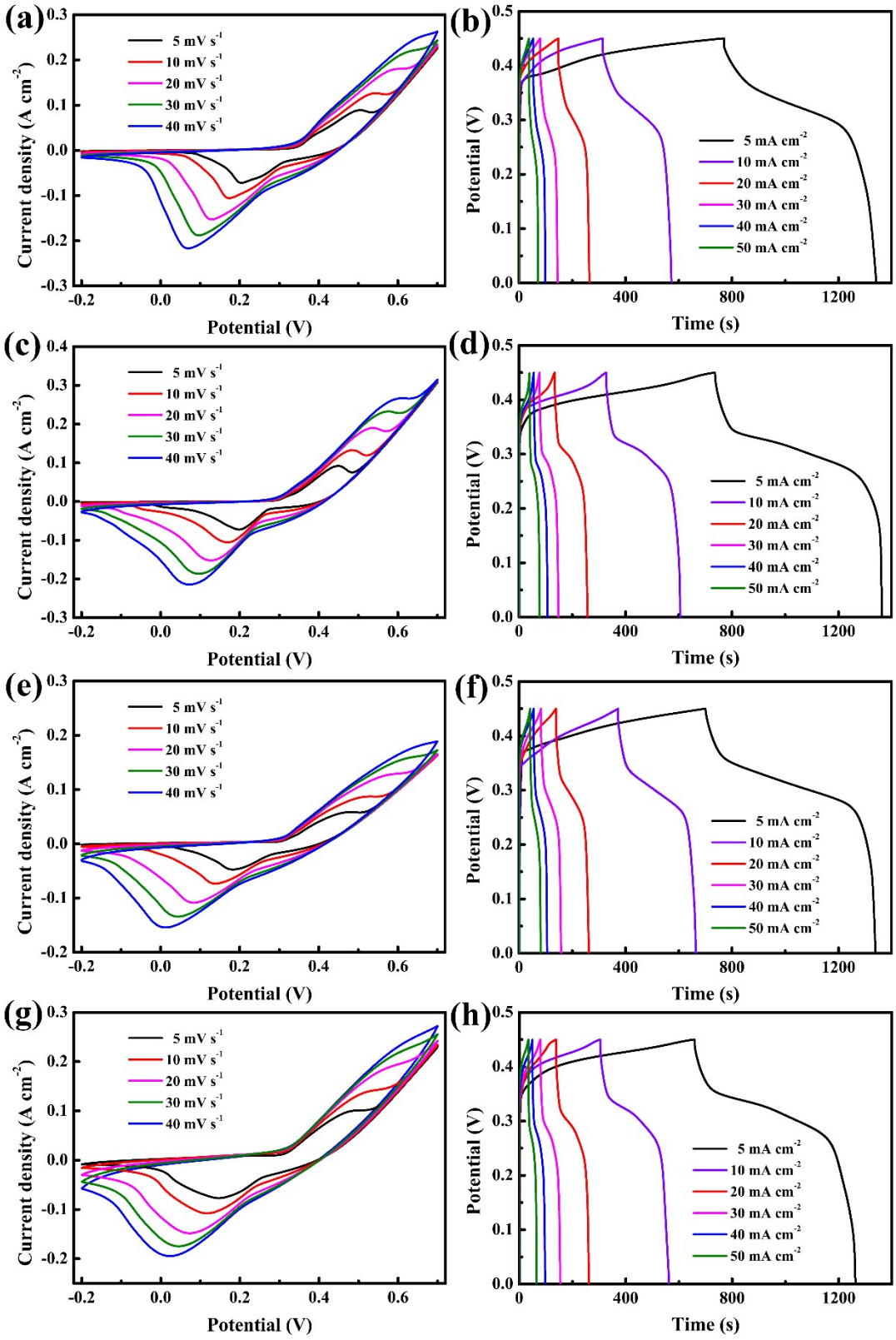

Fig. S10 CV curves (a, c, e and g) at different scan rates and GCD curves at different current densities (b, d, f and h) of (a, b) NFP-1, (c, d) NFP-2, (e, f) NFP-4, and (g, h) NFP-5 electrodes.

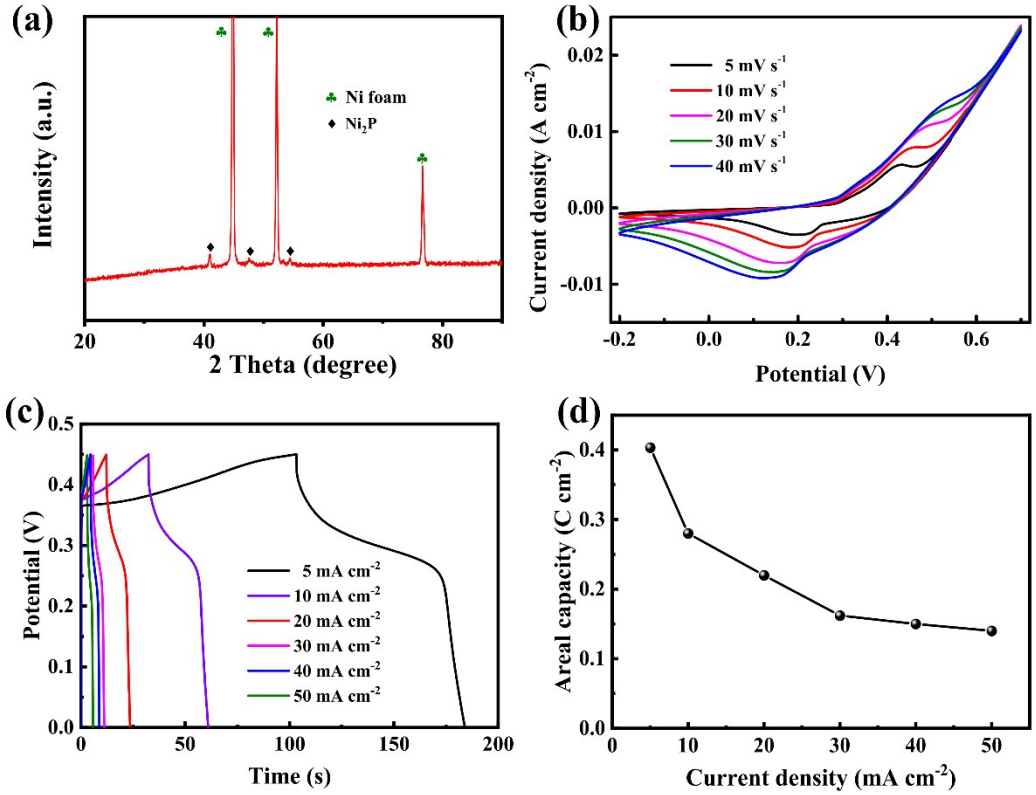

Fig. S11 (a) XRD pattern of the sample-1. (b) CV curves of sample-1 electrode measured at different scan rates in the voltage range of -0.2 ~ 0.7 V. (c) GCD curves of sample-1 at different current densities from 0 to 0.45 V. (d) Specific areal capacities of sample-1 at different current densities.

We fabricated the sample (recorded as sample-1) prepared in a similar way of Ni-Fe-P-350 electrode in the absence of metal sources in hydrothermal reaction. After the same annealing process with the existence of NaH_2PO_2, the XRD test of this sample (recorded as sample-1) was performed (Fig. S11a). The weak diffraction peaks could be ascribed to the Ni_2P (PDF 03-0953) except the peaks of Ni foam (PDF 04-0850), indicating that the Ni foam is partially phosphatized. Then we tested the electrochemical performance of this sample, as shown in Fig. S11b-d. The specific areal capacities of sample-1 are 0.4 to 0.14 C cm^{-2} at current densities of 5 to 50 mA cm^{-2}. The electrochemical properties of the Ni foam after phosphorization are increased than before. Although the Ni-Fe-P-350 nanosheets grow uniformly on the substrate, the open space of the porous network can still store the electrolyte and permeate the surface of

phosphatized Ni foam in the actual electrochemical reactions. So this phosphatized Ni foam could make some positive contributions to the specific capacity of Ni-Fe-P-350 electrode in the electrochemical tests.

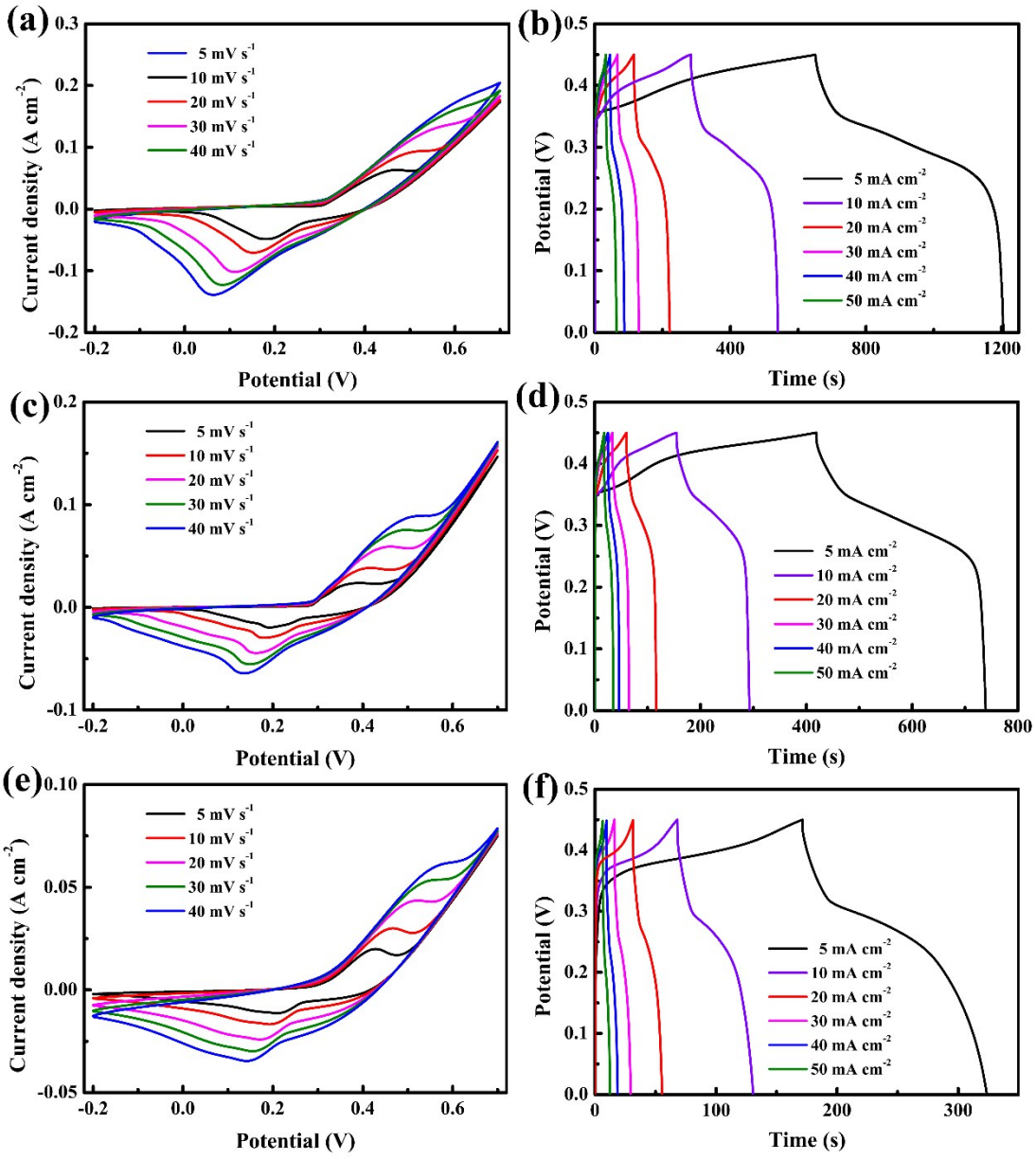

Fig. S12 CV tests (a, c, and e) and GCD tests (b, d, and f) of (a, b) Ni_2P, (c, d) Ni-Fe LDH, and (e, f) Ni-Fe-O electrodes.

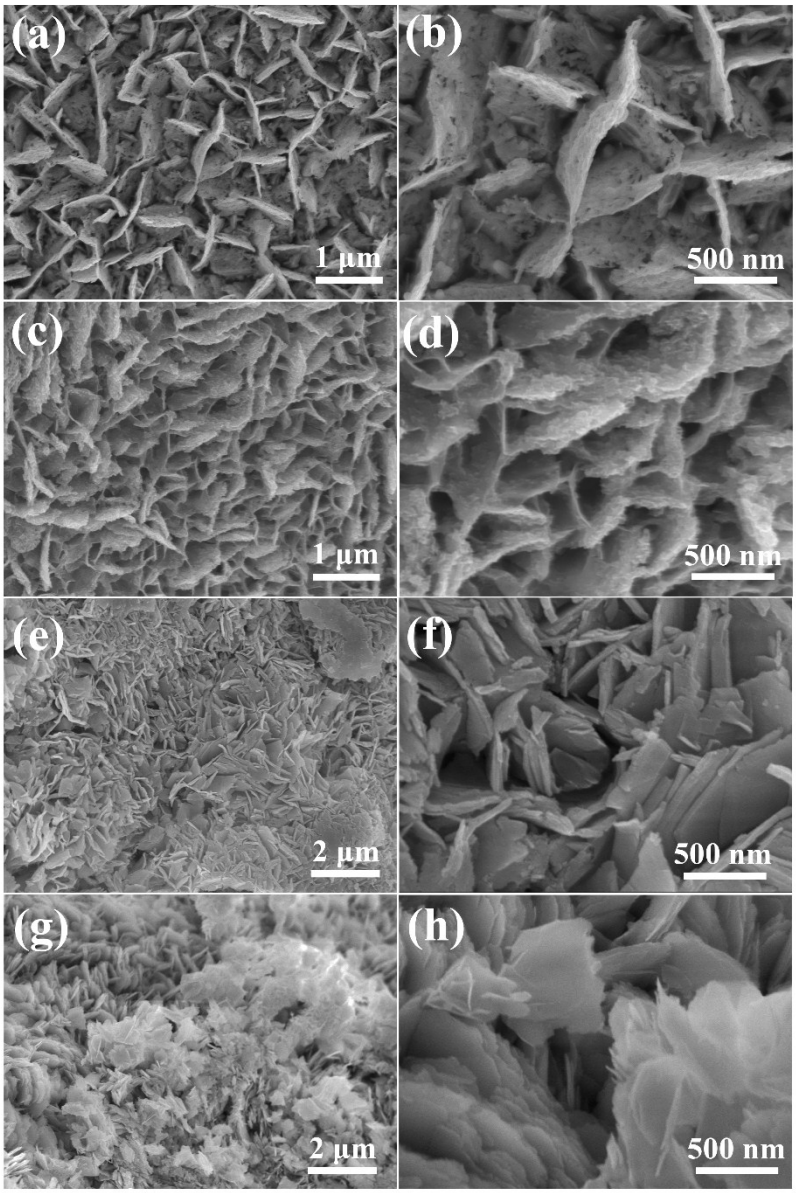

Fig. S13 SEM images of (a-b) Ni-Fe-P-350, (c-d) Ni_2P, (e-f) Ni-Fe LDH, and (g-h) Ni-Fe-O nanosheet arrays after 10000 cycles.

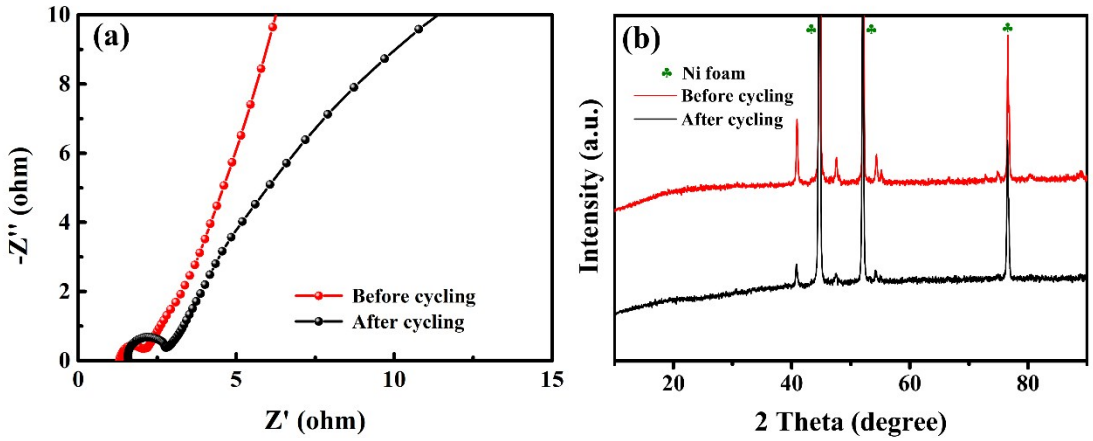

Fig. S14 (a) EIS curves and (b) XRD patterns of Ni-Fe-P-350 electrode before and after 10000 cycles.

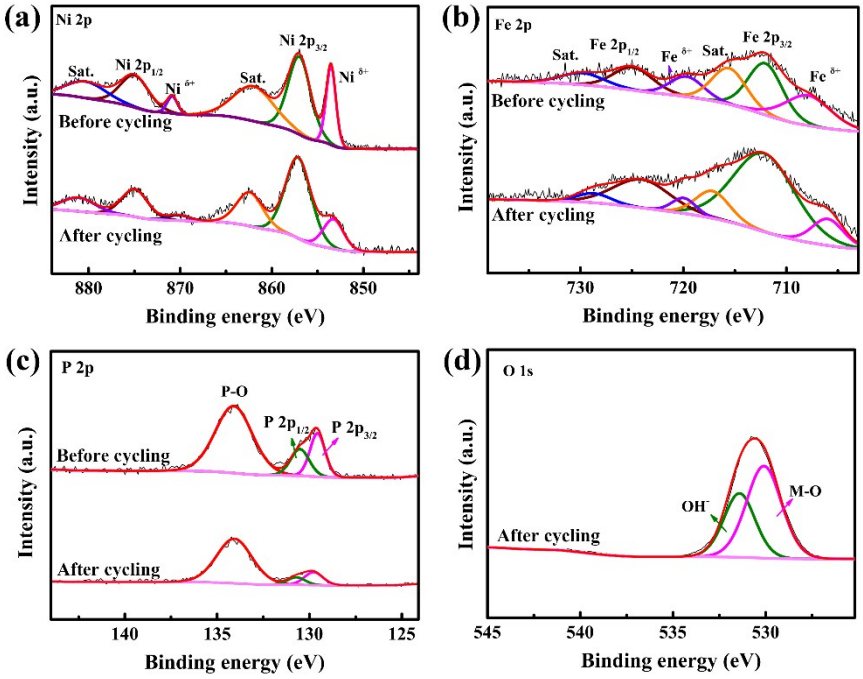

Fig. S15 XPS spectra of (a) Ni 2p, (b) Fe 2p and (c) P 2p of the Ni-Fe-P-350 sample before and after cycling test. (d) XPS spectrum of O 1s of the Ni-Fe-P-350 sample after cycling test.

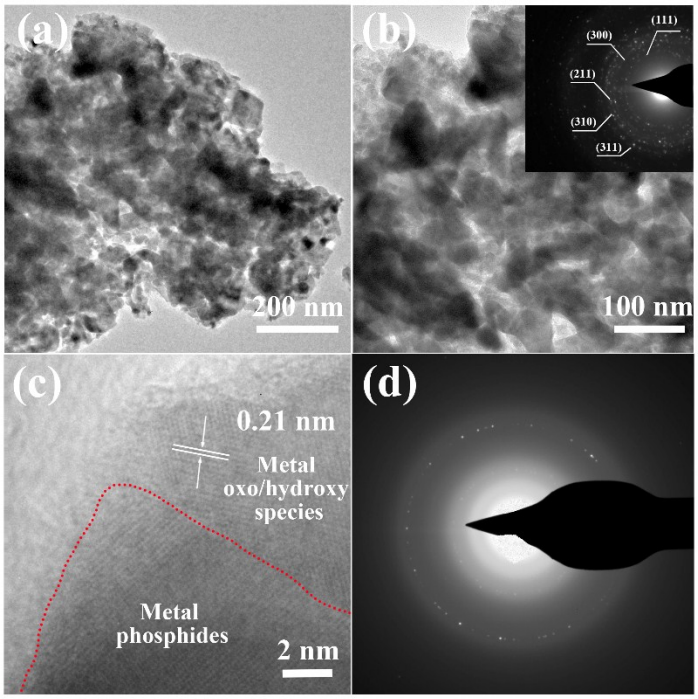

Fig. 16 TEM investigations of the Ni-Fe-P-350 sample after cycling test. (a and b) TEM images (the inset of b shows the SAED pattern of the metal phosphide). (c) HRTEM image. (d) SAED pattern of the generated metal oxo/hydroxyl species.

Fig. S15 shows the XPS spectra of the Ni-Fe-P-350 sample before and after cycling test. As shown in Fig. S15a, the decreased peaks of $Ni^{\delta+}$ at 853.6 and 870.6 eV can be observed after the cycling test compared with the peaks before cycling, indicating that the surface of the phosphide have been oxidized.[1] The $Fe^{\delta+}$ peaks after cycling test shown in Fig. S15b are aslo decreased and the peaks at 712.3 and 724.5 eV increase obviously, which also suggest the oxidation of the surface. The peaks of P $2p_{3/2}$ and P $2p_{1/2}$ (Fig. S15c) which represent the metal-P bonding also exhibit the declined trend. Furthermore, the O 1s spectrum (Fig. S15d) presents two peaks at 530.1 and 531.4 eV which can be ascribed to the oxygen and hydroxyls of the metal oxides/hydroxides generated on the surface after the cycling test.[2] The XPS analyses suggest that the surface oxidation occurred and the metal oxides/hydroxides generated after cycling test. While the metal phosphide still exist in this electrode. These results are similar with the previous report.[3]

Fig. S16 shows the TEM investigations of the Ni-Fe-P-350 sample after cycling test.

The nanosheet of the sample still maintains the porous structure (Fig. S16a and b), which is in good agreement with the SEM results (please see Fig. S13a and b in the Supporting Information). The inset of Fig. S16b displays the SAED pattern and serial annulus express planes of (111), (300), (211), (310) and (311) of the still remaining metal phosphides, indicating the polycrystal structure. The lattice fringe in HRTEM image (Fig. S16c) shows a distance of 0.21 nm which represents the specific facet of metal oxides/hydroxides, suggesting that the oxides/hydroxides have been formed on the surface of the sample.[1, 2, 4] The SAED pattern shown in Fig. S16d illustrates the poor crystallinity and the low content of the metal oxo/hydroxyl species on the surface. The TEM results also verify the surface oxidation and the metal phosphide core still exist, which accord well with the XPS analysis. And the XRD pattern (please see Fig. S14b in the Supporting Information) of the Ni-Fe-P-350 sample after cycling test shows no diffraction peaks of metal oxides/hydroxides. We infer that this is because of the poor crystallization behavior and lower content of metal oxides/hydroxides in comparison with the phosphides, so XRD test cannot detect them. This phenomenon was also reported in another previous article.[5]

The XPS and TEM analyses prove the surface oxidation of the metal phosphide electrode after the cycling test. And the contents of the formed metal oxides/hydroxides are very small. The metal phosphides exist widely as core and host materials beneath the oxidation layer. So the metal phosphides are the main electroactive materials for the contribution of capacitance. In addition, there probably has generated a new metal-P/oxides/hydroxides (M-P/O/OH) heterojunction on the surface of the still existing metal phosphide core, which likely improves the electrochemical activity of the electrode.[4, 5] The electrochemical performance of the Ni-Fe-O and Ni-Fe LDH electrodes (please see Fig. 5 in the manuscript) could attest this point. Without the metal phosphides as the core and host materials, the Ni-Fe-O and Ni-Fe LDH electrodes with poor conductivity exhibit the not satisfactory performance. The metal phosphides may be the ideal and conductive core to accelerate the electron transfer in the electrochemical reactions.[6, 7] In short, the underlying metal phosphides have an important role in the enhancement of the electrochemical behavior for supercapacitors

and make a major contribution for the excellent capacitance.

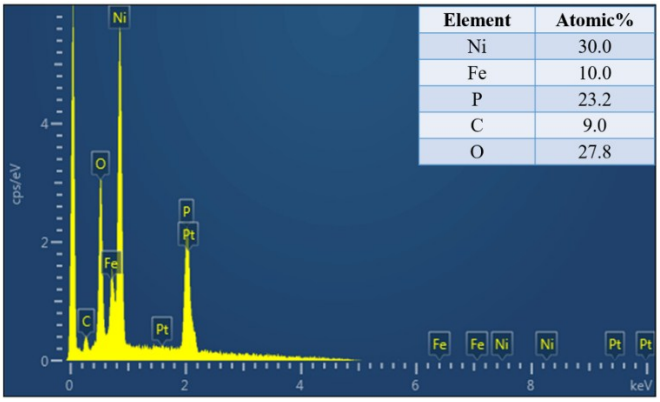

Element	Atomic%
Ni	30.0
Fe	10.0
P	23.2
C	9.0
O	27.8

Fig. S17 EDS spectrum of Ni-Fe-P-350 electrode.

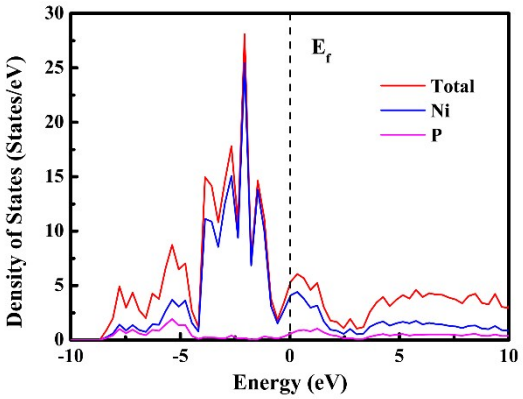

Fig. S18 Total DOS of Ni_2P.

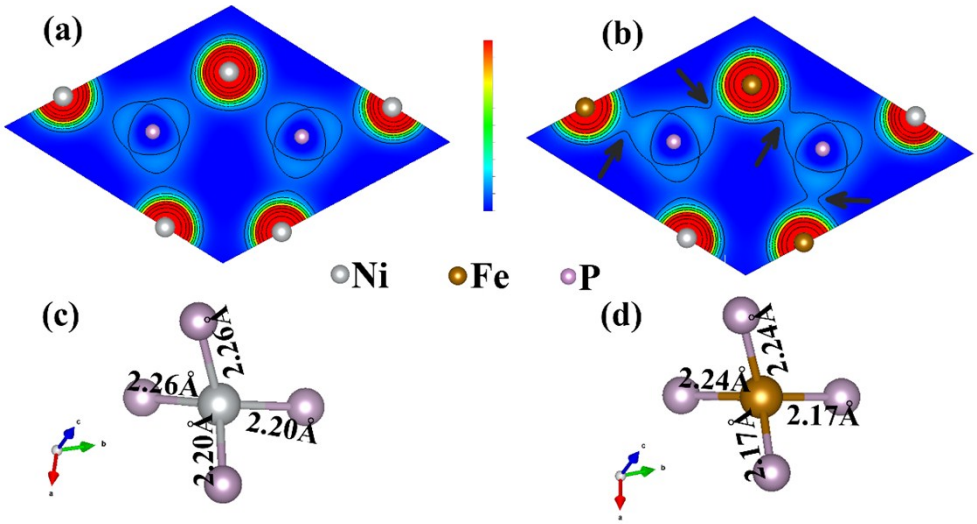

Fig. S19 Electron density distributions of (a) Ni_2P and (b) Ni-Fe-P. The arrows show the increased electron density between Fe and P atoms. The local structures of (c) Ni-P and (d) Fe-P with the values expressing the bond lengths.

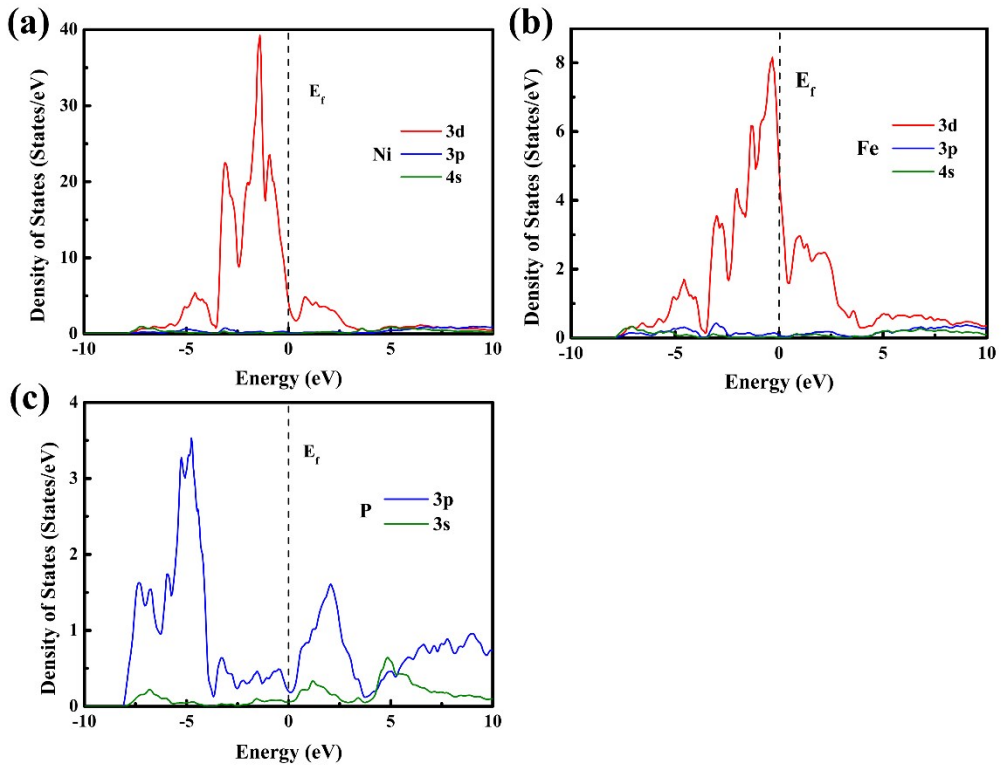

Fig. S20 Partial DOS of (a) Ni, (b) Fe, and (c) P for Ni-Fe-P system.

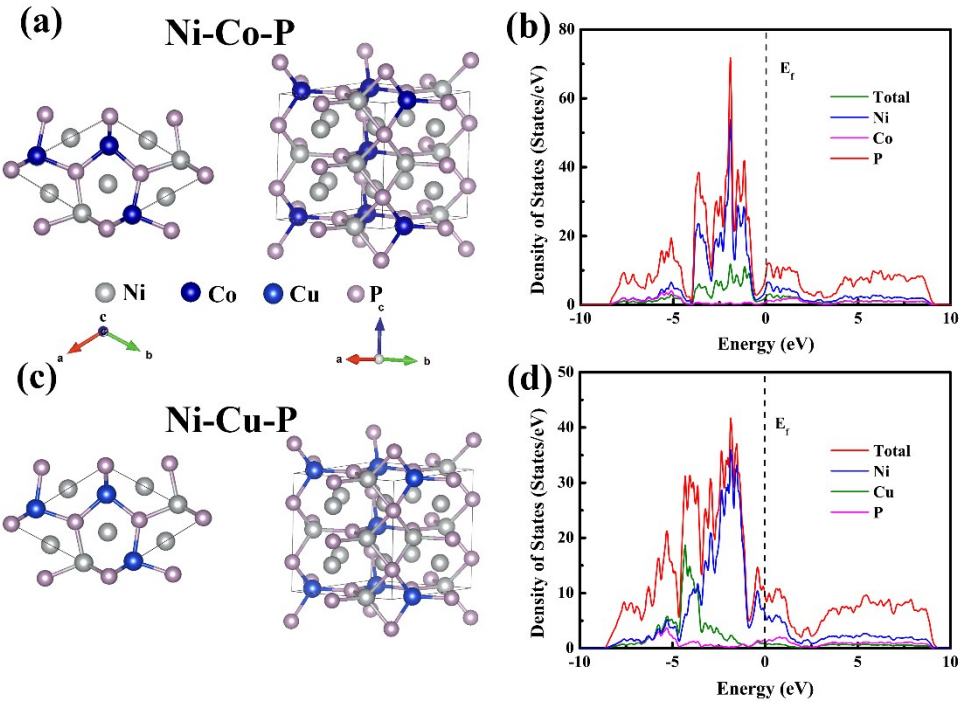

Fig. S21 The crystal structures of (a) Ni-Co-P and (c) Ni-Cu-P at different visual angels. DOS of (b) Ni-Co-P and (d) Ni-Cu-P.

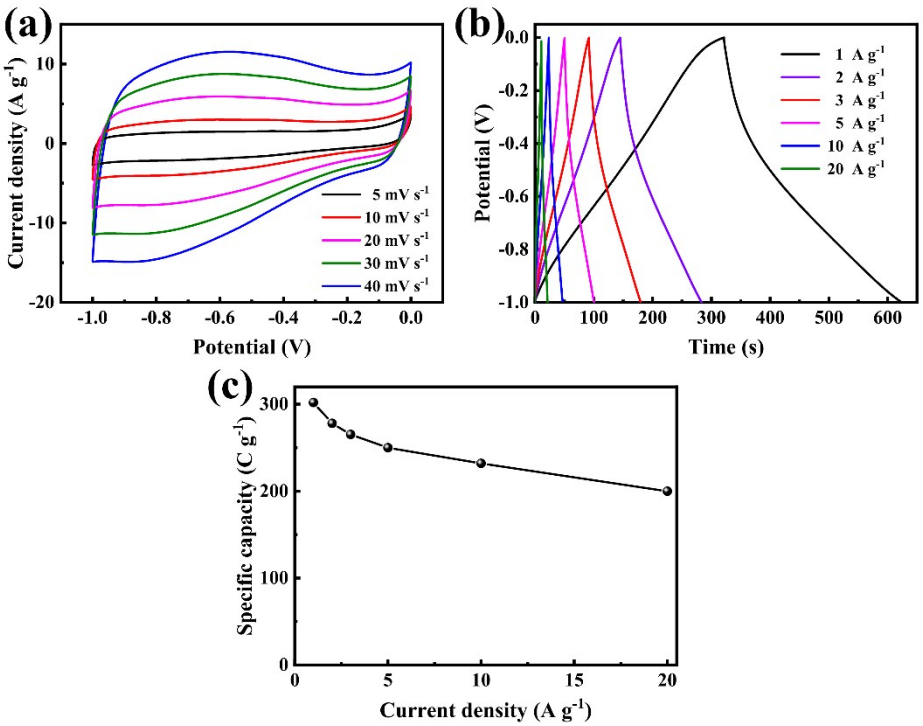

Fig. S22 (a) CV tests of RGO electrode at various sweep rates. (b) GCD tests and (c) specific gravimetric capacities of RGO electrode at various current densities.

Table. S1 The Ni-Fe based phosphides with different Fe contents and the corresponding labels.

Fe/Ni molar ratios (%)	12%	20%	33%	39%	47%
The labels of samples	NFP-1	NFP-2	NFP-3	NFP-4	NFP-5

Table S2. Electrochemical performance of the Ni-Fe-P electrode compared with the similar reported materials.

Electrode materials	**Specific capacity**	**Stability (Cycles)**	**Ref.**
Ni-Fe-P	1358 C g^{-1}/ 3018 F g^{-1} (5 mA cm^{-2})	94.7% (10000 cycles)	This work
NiCoP/NiCo-OH	1100 F g^{-1} (1 A g^{-1})	88% (1000 cycles)	[8]
Ni_xP_y	2544 F g^{-1} (2 A g^{-1})	90.9% (5000 cycles)	[9]
CuCoP	1946 F g^{-1} (5 mA cm^{-2})	92.7% (6000 cycles)	[10]
Cu_3P	300.9 F g^{-1} (2.5 mA cm^{-2})	/	[11]
NiCoOP@C	2638 F g^{-1} (1 A g^{-1})	84% (3000 cycles)	[12]
NiCoP	1427.5 F g^{-1} (1 A g^{-1})	71.8% (3000 cycles)	[13]
Ni-P	1597.5 F g^{-1} (0.5 A g^{-1})	71.4% (1000 cycles)	[14]
Ni-P@$NiCo_2O_4$	1240 F g^{-1} (1 A g^{-1})	/	[15]
NiCoP	1153 F g^{-1} (1 A g^{-1})	97% (7000 cycles)	[16]
$Ni_{12}P_5$	949 F g^{-1} (1 A g^{-1})	81% (2000 cycles)	[17]
Co_2P	416 F g^{-1} (1 A g^{-1})	/	[18]
CoP	447.5 F g^{-1} (1 A g^{-1})	84.3% (5000 cycles)	[19]

Table S3. Electrochemical performance of the Ni-Fe-P//RGO HSC device compared with the similar reports.

HSC device	Maximum energy density	Maximum power density	Stability (Cycles)	Ref.
Ni-Fe-P//RGO	65.1 Wh kg^{-1}	19.7 kW kg^{-1}	91.5% (10000 cycles)	This work
NiCoP/NiCo-OH //porous carbon	34 Wh kg^{-1}	11.6 kW kg^{-1}	92% (1000 cycles)	[8]
Cu_3P //CNT	44.6 Wh kg^{-1}	17 kW kg^{-1}	81.9% (5000 cycles)	[11]
NiCoOP@C //AC	39.4 Wh kg^{-1}	7.5 kW kg^{-1}	70.6% (7000 cycles)	[12]
NiCoP //AC	32 Wh kg^{-1}	5.6 kW kg^{-1}	91.8% (3000 cycles)	[13]
Ni-P //AC	29.2 Wh kg^{-1}	8 kW kg^{-1}	84.5% (1000 cycles)	[14]
Ni-P@$NiCo_2O_4$//AC	13.3 Wh kg^{-1}	5.7 kW kg^{-1}	78.3% (10000 cycles)	[15]
NiP@CoAl-LDH //AC	37.18 Wh kg^{-1}	4.68 kW kg^{-1}	95.5% (4000 cycles)	[20]
NiCoP //AC	32.9 Wh kg^{-1}	8.5 kW kg^{-1}	83% (5000 cycles)	[21]
Co_2P//graphene	24 Wh kg^{-1}	6 kW kg^{-1}	97% (6000 cycles)	[18]
Ni_8-Co_1-P//AC	22.8 Wh kg^{-1}	4.32 kW kg^{-1}	100% (5000 cycles)	[22]
$Ni_3P_2O_8$//$Fe_3P_2O_8 \cdot 8H_2O$	32.6 Wh kg^{-1}	3.35 kW kg^{-1}	81% (10000 cycles)	[23]
CoP//AC	19 Wh kg^{-1}	8.5 kW kg^{-1}	96.7% (5000 cycles)	[19]

References

1. J. Li, M. Yan, X. Zhou, Z.-Q. Huang, Z. Xia, C.-R. Chang, Y. Ma and Y. Qu, *Adv. Funct. Mater.*, 2016, **26**, 6785-6796.
2. X.-Y. Yu, Y. Feng, B. Guan, X. W. Lou and U. Paik, *Energ. Environ. Sci.*, 2016, **9**, 1246-1250.
3. T. T. Nguyen, J. Balamurugan, N. H. Kim and J. H. Lee, *J. Mater. Chem. A*, 2018, **6**, 8669-8681.
4. L.-A. Stern, L. Feng, F. Song and X. Hu, *Energ. Environ. Sci.*, 2015, **8**, 2347-2351.
5. X. Wang, W. Li, D. Xiong, D. Y. Petrovykh and L. Liu, *Adv. Funct. Mater.*, 2016, **26**, 4067-4077.
6. M. Gong, W. Zhou, M.-C. Tsai, J. Zhou, M. Guan, M.-C. Lin, B. Zhang, Y. Hu, D.-Y. Wang and J. Yang, S. J. Pennycook, B. –J. Hwang and H. Dai, *Nat. commun.*, 2014, **5**, 4695.
7. L. Trotochaud, S. L. Young, J. K. Ranney and S. W. Boettcher, *J. Am. Chem. Soc.*, 2014, **136**, 6744-6753.
8. X. Li, H. Wu, A. M. Elshahawy, L. Wang, S. J. Pennycook, C. Guan and J. Wang, *Adv. Funct. Mater.*, 2018, **28**, 1800036.
9. S. Liu, K. V. Sankar, A. Kundu, M. Ma, J. -Y. Kwon and S. C. Jun, *ACS Appl. Mater. Interfaces*, 2017, **9**, 21829-21838.
10. S. E. Moosavifard, S. K. Kaverlavani, J. Shamsi and A. Bakouei, *J. Mater. Chem. A*, 2017, **5**, 18429-18433.
11. Y.-C. Chen, Z.-B. Chen, Y.-G. Lin and Y.-K. Hsu, *ACS Sustain. Chem. Eng.*, 2017, **5**, 3863-3870.
12. Y. Shao, Y. Zhao, H. Li and C. Xu, *ACS Appl. Mater. Interfaces*, 2016, **8**, 35368-35376.
13. Y.-M. Hu, M.-C. Liu, Y.-X. Hu, Q.-Q. Yang, L.-B. Kong and L. Kang, *Electrochim. Acta*, 2016, **215**, 114-125.
14. D. Wang, L.-B. Kong, M.-C. Liu, W.-B. Zhang, Y.-C. Luo and L. Kang, *J. Power Sources*, 2015, **274**, 1107-1113.
15. X. Li, R. Ding, L. Yi, W. Shi, Q. Xu and E. Liu, *Electrochim. Acta*, 2016, **222**, 1169-1175.
16. Y. Jin, C. Zhao, Q. Jiang and C. Ji, *Appl. Surf. Sci.*, 2018, **450**, 170-179.
17. H. Wan, L. Li, Y. Chen, J. Gong, M. Duan, C. Liu, J. Zhang and H. Wang, *Electrochim. Acta*, 2017, **229**, 380-386.
18. X. Chen, M. Cheng, D. Chen and R. Wang, *ACS Appl. Mater. Interfaces*, 2016, **8**, 3892-3900.
19. Y. Hu, M. Liu, Q. Yang, L. Kong and L. Kang, *J. Energy Chem.*, 2017, **26**, 49-55.
20. S. Wang, Z. Huang, R. Li, X. Zheng, F. Lu and T. He, *Electrochim. A*, 2016, **204**, 160-168.
21. H. Liang, C. Xia, Q. Jiang, A. N. Gandi, U. Schwingenschlögl and H. N. Alshareef, *Nano Energy*, 2017, **35**, 331-340.
22. R. Ding, X. Li, W. Shi, Q. Xu and E. Liu, *Chem. Eng. J.*, 2017, **320**, 376-388.
23. M. Liu, J. Li, W. Han and L. Kang, *J. Energy Chem.*, 2016, **25**, 601-608.